Scripta Materialia 201 (2021) 113978

Contents lists available at ScienceDirect

Scripta Materialia

journal homepage: www.elsevier.com/locate/scriptamat

Real-time visualization of particle evolution during reactive flux-assisted processing of aluminum melts

C.W. Reese[a,*], A. Gladstein[a], P. Shevchenko[b], X. Xiao[c], A.J. Shahani[a], A.I. Taub[a,d]

[a] Materials Science & Engineering, University of Michigan, 2300 Hayward St, HH Dow Bldg, Rm 2062, Ann Arbor, MI 48109, USA
[b] Advanced Photon Source, Argonne National Laboratory, Argonne, IL 60439, USA
[c] National Synchrotron Light Source II, Brookhaven National Laboratory, Upton, NY 11973, USA
[d] Mechanical Engineering, University of Michigan, Ann Arbor, MI 48109, USA

ARTICLE INFO

Article history:
Received 4 March 2021
Revised 26 April 2021
Accepted 29 April 2021

Keywords:
Metal matrix composites (mmc)
In situ characterization
Nucleation and growth
Synchrotron x-ray radiation
Carbides

ABSTRACT

A multi-modal, multi-scale correlative tomography investigation of Al-TiC metal matrix composites processed *via* flux-assisted reaction synthesis is reported. Synchrotron X-ray microradiography is utilized to visualize the reaction and particle evolution in real-time. Changes in particle diameter and areal number density suggest that the process is nucleation- rather than growth-dominated. At 950 °C, the bulk of the reaction takes place in a relatively short time span of less than 600 s. The microstructure is imaged at higher resolution in 2D (scanning electron microscopy) and 3D (synchrotron X-ray nanotomography), revealing the formation of carbide particles with a hexagonal platelet morphology. We propose that the morphology arises due to the incorporation of Si impurities during the experiment. It is expected that the correlative tomography workflow and analysis may guide future metal matrix composite (MMC) processing strategies.

To meet the ever-increasing demands for improved fuel economy in the automotive and aerospace industries, Al-alloys have been used extensively owing to their high strength-to-weight ratio. However, thermal stability of mechanical properties has limited their usage in key components operating in elevated temperature environments. Al-based metal matrix composites (MMCs) have been shown to exhibit improved elevated temperature properties, where careful tuning of the particulate reinforcement characteristics (*i.e.*, size, volume fraction, morphology) is tied to improved mechanical performance [1,2]. MMCs are commonly manufactured *via ex situ* methods, wherein pre-made particles are mixed into the matrix. Although particle size and amount can easily be controlled prior to melt addition using *ex situ* approaches, undesirable particle-matrix interfacial reactions [3–5] and poor particle-matrix wetting [6,7] have made incorporation of the particles in large-scale processing difficult. Alternatively, *in situ* methods utilizing reactive processes [1,8] can circumvent some of these difficulties *via* direct particle creation in the melt. However, *in situ* particle formation is typically a complex process [9–11] involving intermediate reaction steps, parallel reaction pathways leading to different morphologies, and generation of undesirable secondary phases, all of which may have an impact on the microstructure and corresponding mechanical properties. An understanding of the particle formation kinetics is critical for microstructural control of *in situ* MMCs.

One promising *in situ* approach for synthesis of Al-TiC MMCs involves reacting a mixture of C powder and a molten salt-based flux (dipotassium titanium hexafluoride, K_2TiF_6) in an Al melt [12,13]. The formation of TiC is hypothesized to occur *via* a reaction between free Ti atoms, released during flux reduction by the liquid Al, and solid C particles; however, the underlying mechanisms and kinetics are still an open question [13–16]. This is because the conventional approach to understanding reactive MMC processing methods has largely relied on empirical correlations of microstructural attributes in as-solidified specimens, with melt processing parameters. This makes it challenging to reconstruct the dynamical events that led to the formation of TiC particles. For example, it is not clear if the anomalously large, μm-sized TiC domains seen in *post mortem* studies [16,17] are due to agglomeration of nm-sized particles or sustained growth of a single particle. *In situ* monitoring techniques such as synchrotron X-ray diffraction [18–21] and neutron diffraction [22–24] offer a route to characterize the reaction in real-time. While these approaches yield some valuable information, they may fail to capture the full complexity and heterogeneity of the microstructure. By contrast, correlative X-ray tomography offers a direct view of material processing across multiple length- and time-scales by leveraging coordinated characterization techniques [25–28]. Here, we combine observations from synchrotron

---

[*] Corresponding author.
E-mail address: reesecw@umich.edu (C.W. Reese).

https://doi.org/10.1016/j.scriptamat.2021.113978

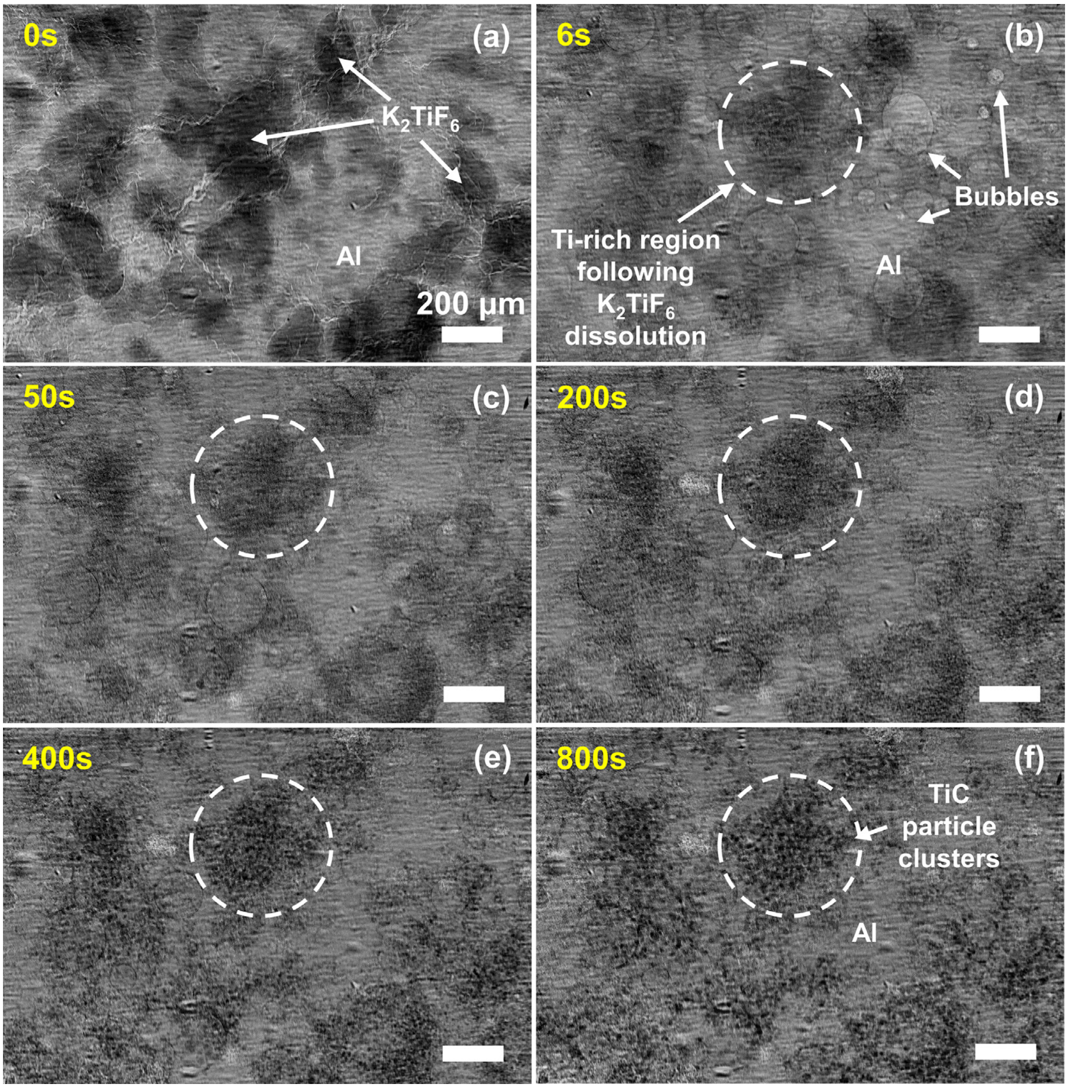

Fig. 1. X-ray microradiographs showing microstructural evolution during flux-assisted processing of Al melts. (a) Upon insertion of an Al, C, K_2TiF_6 powder compact into a furnace at 950 °C, unreacted flux particles are visible immediately prior to Al melting (denoted as 0 s). (b) At 6 s, the Al has melted (as indicated by the bubbles) and flux particles begin to dissolve, leaving behind presumably Ti-rich regions. (c-f) At later time steps ($\geq$50 s), dark carbide particles or particle clusters begin to appear from Ti-rich regions and increase in density and diameter over time.

X-ray microradiography (XRR) [29–32] and nanotomography based on the transmission X-ray microscope (TXM) [33–36] to provide new insights on the kinetics of the flux-assisted reaction synthesis process. We observe carbide particle formation to be nucleation- rather than growth-dominated, with the reaction taking place in <600 s at 950 °C. The implications of our observations on the particle formation mechanisms are discussed. We also detect the presence of Si and discuss its impact on particle morphology and growth.

Samples for synchrotron XRR experiments were prepared from K_2TiF_6 flux (>100 μm) and C (~10 μm, 99.95% purity) powders, targeting stoichiometric TiC, and mixed with 2 × Al (~30 μm, 99.5% purity) powder by weight. Powders were consolidated into chips (~200–250 μm thickness) *via* cold pressing at ~200 MPa and sandwiched between 100 μm quartz (SiO_2) coverslips (See Supplementary Information (SI) for more details). Synchrotron XRR experiments were conducted at Sector 2-BM at the Advanced Photon Source (APS) at Argonne National Laboratory (Lemont, IL, USA). A monochromatic X-ray beam operating at 20 keV was focused onto the samples and X-rays were converted to visible light using a 25 μm thick LuAG:Ce scintillator. Images were collected using a FLIR Oryx CCD with a 5 × magnifying objective lens, yielding pixel sizes of 0.69^2 μm^2 within a field-of-view (FOV) of 1689 × 1413 μm^2. Real-time XRR experiments of the flux-assisted reaction were carried out in a resistance furnace. The furnace was equilibrated at a chamber temperature of 950 °C and rapidly lowered onto the sample where melting and reaction were observed. Radiographs were collected for approximately 30 min with an exposure of 200 ms. The furnace was subsequently raised, and the reacted samples solidified quickly in air. The generalized radiograph processing workflow consisted of normalization using dark- and white-field images, de-striping of horizontal line artifacts [37], phase segmentation *via* Zeiss Zen Intellesis deep learning analysis software, and drift correction *via* the StackReg and TurboReg [38] ImageJ registration plugins. Individual particle identification and quantification were carried out using the Image Processing toolbox available in MATLAB 2020a, namely morphological filtering and further watershed transformation-based segmentation (See SI for additional details).

To examine the as-solidified microstructure corresponding to the XRR field-of-view (FOV), characterization was performed using a Tescan MIRA3 field emission gun (FEG) SEM operating in backscatter electron (BSE) mode at 15 kV and a beam intensity of 12–15, while an integrated EDAX energy dispersive spectroscopy (EDS) system was utilized for chemical identification. To ensure consistency between the surface and bulk microstructures at nanometer length-scales, the same material was also visualized using TXM. Samples were prepared by sectioning an approximately 0.5^2 mm^2 piece (from the sample edge, away from the XRR FOV) with a razor blade and bonding to the end of a steel needle with conductive Ag paint. TXM micropillar specimens approximately 40 μm in diameter and 100 μm in height were fabricated from the mounted samples *via* plasma Xe$^+$ ion milling with an FEI Helios G4 P-FIB operating at 30 kV and 2.5 μA. To ensure visualization of the bulk, samples were mounted and milled such that the long axis of the micropillar corresponds to the through-thickness direction of the XRR sample. Nano-scale tomography characterization was conducted with the TXM at the Full-field X-ray Imaging beamline 18-ID at the National Synchrotron Light Source II (Upton, NY, USA). The tomography scans were conducted at 7 keV. A zone plate with outmost zone width of 30 nm was used as the X-ray objective lens to magnify the X-ray absorption images of the sample. The X-ray images were collected with a lens-couple X-ray detector with CeI scintillator. The overall magnification was 329 ×. Pixel size on the detector was 19.8^2 nm^2 and FOV measured 50.6^2 µm^2. A more detailed description of the TXM setup is available elsewhere [39]. In the TXM experiment, the sample was rotated at 1°/s from 0 to 180°, with an exposure of 0.1 s. Attenuation contrast between the TiC platelets and Al matrix allowed them to be readily distinguished. TXM projection data was reconstructed *via* the Gridrec algorithm with Parzen filtering [40,41] within TomoPy [42] and subsequently segmented and visualized using the Image Processing Toolbox in MATLAB 2020b (See SI for additional details).

The results of our *in situ* XRR visualization are shown in Fig. 1 as a sequence of flat-field corrected and de-striped X-ray radiographs. In Fig. 1(a), the sample has not yet melted following insertion into the furnace; dark K_2TiF_6 flux particles are visible against the lighter matrix owing to the attenuation contrast of elemental Ti. This particular frame is taken to be the 0 s mark. Within approximately 4–6 s, the Al melts and apparently begins to react with K_2TiF_6; at this stage, bubbles as well as shrinkage and interface-motion-induced blurring of flux particles becomes apparent (Fig. 1(b)). At 50 s (Fig. 1(c)), dark regions remain near the initial flux-particle sites and correspond to Ti solute-rich areas following reaction of K_2TiF_6. Subsequently (Fig. 1(d–f), 299–800 s), small dark spots, confirmed later to be carbide particles, appear in and around the Ti-rich regions and gradually increase in density and size over time.

Fig. 2 shows the time-evolution of average diameter and areal density of the particles. It is important to note that an individual particle is identified as a connected component (*i.e.*, a group of adjoining pixels are considered connected if any of their edges or corners touch along the horizontal, vertical, or diagonal direction) *via* the image processing techniques described in the SI. In Fig. 2(a), the particle diameter is observed to increase exponentially, reaching an asymptote of ~10 μm in 600 s. Similarly, the areal number density increases exponentially, reaching an asymptote of ~2×10^3 mm^{-2} in 200 s (Fig. 2(b)). Assuming a simple exponential fit for reaction-controlled nucleation, the time constants (denoted here as τ) for the increase in areal density and diameter are calculated as 241 s and 49 s respectively.

To link the radiographic features (*e.g.*, dark spots) to chemical phases, we inspect the post-reacted sample in the same FOV that was visualized by XRR. Fig. 3(a) shows an SEM micrograph of the Al-TiC MMC after reaction, where both surface oxides (darkest gray areas) and a large number of faceted TiC-based particles or platelets (light gray clusters) are observed. A representative higher magnification micrograph of the particles is shown in Fig. 3(b), with the corresponding point EDS spectra identifying Ti, C, and Si shown in the inset. The particles exhibit six-fold faceting, or a hexagonal plate morphology, with an average, equivalent particle diameter of 3.65 ± 1.44 μm and an average facet length of 1.82 ± 0.72 μm (in the plane of the plate). It is worth noting the discrepancy in particle diameter measured from XRR at the long-time limit (Fig. 2(a)) and that retrieved from SEM (Fig. 3). This may be due to the projection geometry of XRR, wherein slightly overlapping or shadowing particles cannot be easily separated through image processing; such overlaps may arise through particle agglomeration or clustering. Probing the bulk microstructure in 3D *via* TXM also reveals faceted particles, suggesting that the platelets are not isolated to the surface (see Fig. 3(c)). 3D TXM visualization shows the appearance of stepped particles, presumably similar to the “clusters” seen in Fig. 3(b) (one of which is identified at the red dot). The steps are the distinguishing features of the connected components or particles, giving way to a non-convex morphology (see inset in Fig. 3(c)).

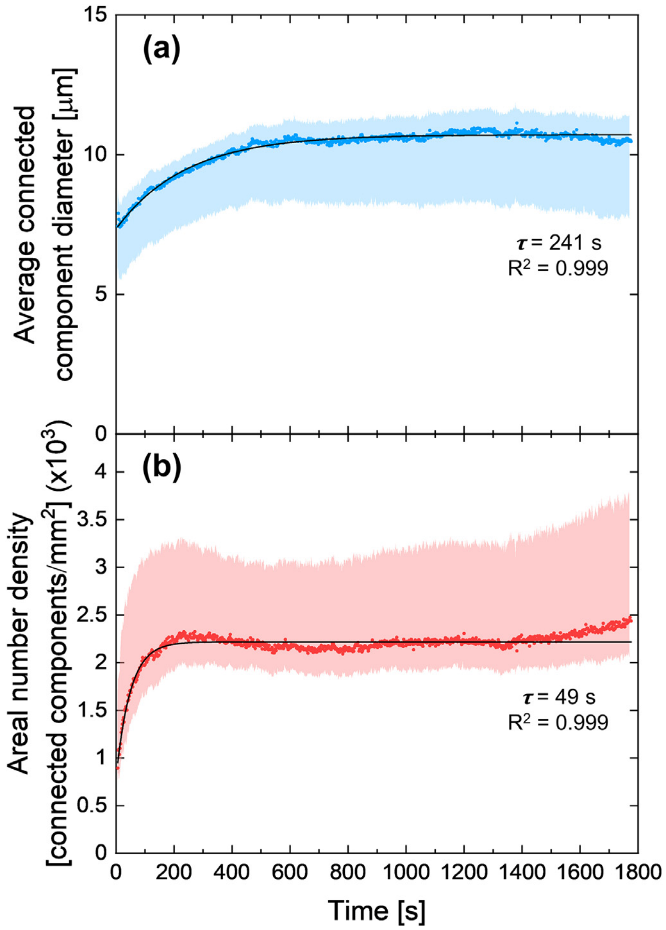

Fig. 2. Kinetics of particle formation. Change in (a) average connected component (particle) diameter and (b) areal number density of connected components (particles) over time, as calculated from the X-ray microradiographs. A connected component is defined as a group of adjoining pixels with any of their edges or corners touching along the horizontal, vertical, or diagonal direction. The baseline (dark colored) curve for both plots was calculated by using a morphological filter with kernel diameter of 2.76 μm, slightly smaller than the average particle diameter determined from SEM, *cf.* Fig. 3). Error bands represent the same calculations but with other choices of kernel diameter, ranging from 1.38 to 4.14 μm. The black solid lines in both (a) and (b) represent exponential decay fits to the baseline curves and τ denotes the corresponding time constants from fitting. The apparent increase in areal number density and decrease in particle diameter at the later time steps (>1400s) are likely an artifact of increased background noise at the longest experiment times.

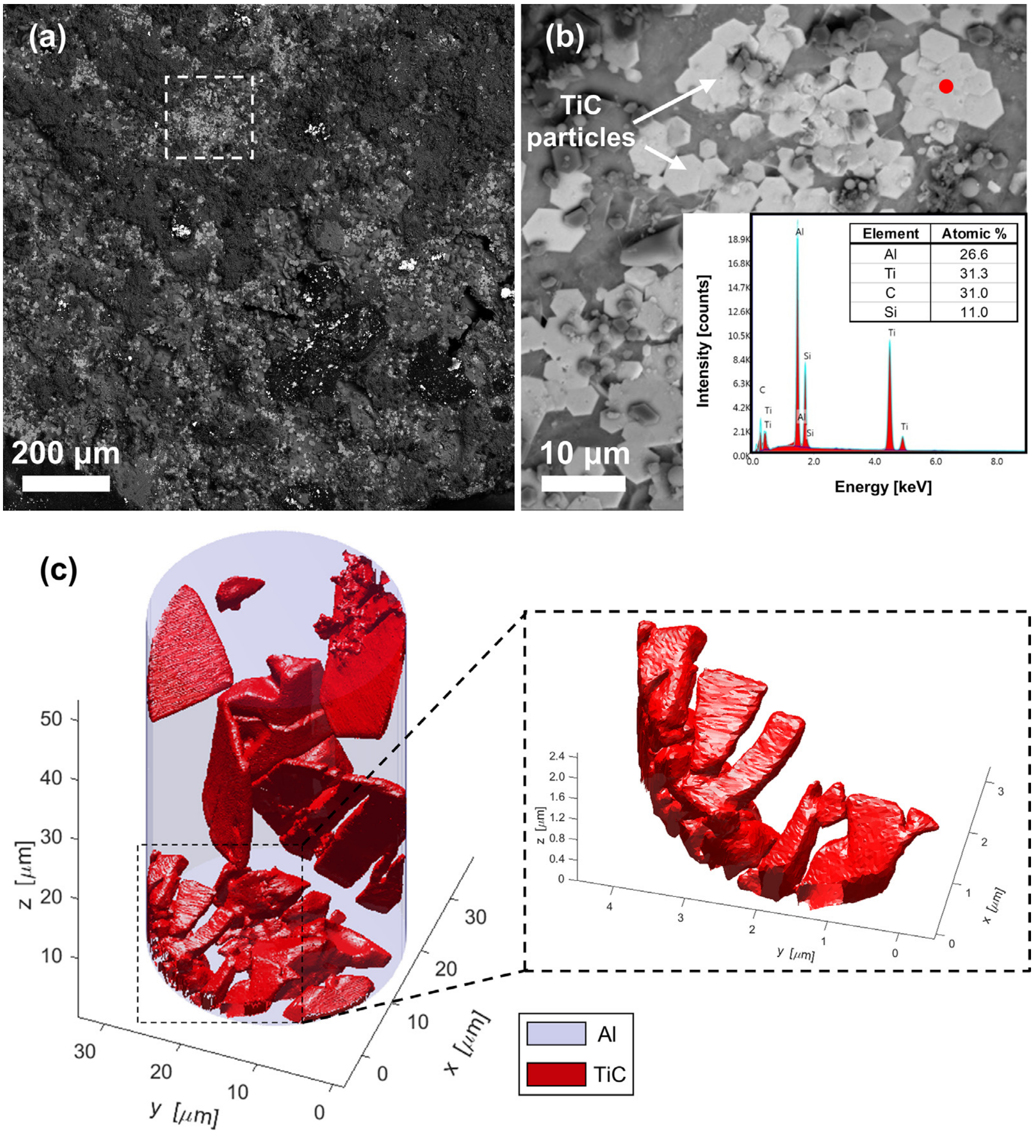

Fig. 3. Microstructural observations of the Al-TiC MMC reacted in the XRR experiments. (a) BSE SEM micrograph of the sample surface in the region corresponding to the XRR FOV. (b) Representative higher magnification BSE SEM image of the sample surface (corresponding to the boxed region in (a)) showing carbide particles/platelets. A spot EDS spectrum taken from the red dot in (b) is shown as an inset. (c) 3D volume rendering of reconstructed TXM data showing a cylindrical field-of-view with TiC particles/platelets (red) in an aluminum matrix (blue). A higher magnification rendering of a stepped, faceted particle is shown as an inset (c, right) (For interpretation of the references to color in this figure legend, the reader is referred to the web version of this article.).

For flux-assisted reaction synthesis in the Ti-C system, previous studies have largely reported particles with a more rounded morphology [12,13] as contrasted with the hexagonal platelets in our study. Faceting of TiC particles has been shown to correspond to the degree of particle off-stoichiometry (*i.e.*, TiC_x), owing to changes in the (100) and (111) relative surface energies with changing ratios of C/Ti [43,44]. However, TiC platelets specifically have been attributed to the incorporation of impurities such as Si [45–47] or B [48], and platelets forming during flux-assisted synthesis in Si-containing base alloys have recently been reported elsewhere [10]. The platelets are hypothesized to be hexagonal in shape resulting from growth along the {110} facets and suppressed growth on the {111} basal planes [44], which is presumably due to an increased density of stacking faults induced by Si-impurities [46,49,50]. Si has also been reported to induce internal defects within TiC, either in the form of microtwins [46] or the precipitation of MAX phases [51–54] (*e.g.*, Ti_3SiC_2 [55]) depending on the local degree of Ti/C off-stoichiometry [49]. Both types of defects have been observed to lead to stacked or stepped platelet morphologies [46,52]. The Si peak observed in the spot EDS (Fig. 2(b)) supports this idea of an impurity-modified microstructure, although we reserve detailed analysis for future work. Furthermore, the non-convex morphology observed in the TXM (Fig. 2(c)) would also be consistent with a defect (*e.g.*, stacking fault) induced crystal shape. Indeed, the stepped growth seen here is reminiscent of the spiral terraces that are responsible for growth of SiC in the form of nanobelts [56]. Although no Si was used in the initial powder sample preparation, presumably a small amount of contamination may have occurred owing to a reaction between the melt and quartz coverslips used to protect the sample during XRR. Reaction between molten Al and SiO_2 has been reported at temperatures as low as 700 °C [57]. Breakdown of SiO_2 (quartz) by the K_2TiF_6 flux is another possibility and previous studies have reported SiO_2 dissolution in the presence of other fluoride-based salts (*e.g.*, K_2SiF_6) [58]. Furthermore, at 950 °C it is also expected that Si impurities would diffuse relatively quickly [59] through the thin, molten sample (characteristic diffusion time of <10 s in a sample of thickness 250 μm, relative to the 30 min duration of the experiment).

Referring to Fig. 2, it is apparent that the bulk of the reaction takes place in approximately the first 200–600 s. This may be particularly relevant for informing future bulk MMC processing, both for tuning particle properties (*e.g.*, size and volume fraction), as well as mitigating detrimental time-dependent phenomenon such as grain refinement fading. It is worth noting that the particle diameter evolution (*i.e.*, growth) curve in particular is not likely driven by agglomeration (the interparticle centroid spacings remain unchanged in time, see SI), nor driven by particle redistribution owing to convective flow (given the thin sample dimensions). Thus, comparison of the time constants associated with the evolution of particle number density and diameter (*i.e.*, 49 s and 241 s, respectively) suggests that the reaction is dominated by nucleation rather than growth (*i.e.*, the smaller number density time constant implies particles are nucleating faster than they grow). If we accept that particle growth is nucleation dominated, the hypothesized formation mechanism supposes that C particles will act as nucleation sites for reaction with Ti solute atoms. While the C particles cannot be directly observed, owing to the relatively low X-ray attenuation of elemental C [60], the X-ray radiographs do suggest that particle nucleation is associated with the Ti-rich regions following K_2TiF_6 reaction with Al (see Fig. 1). Given the negligible solubility of C in Al [61] and the poor wettability between C and Al [62] under these experimental conditions, it stands to reason then that TiC nucleation occurs between C particles and Ti solutes inside the reacted molten salt regions. Particles can subsequently incorporate into the melt after the formation of some initial TiC layer, which aids in wetting with Al [13,15]. It is also interesting to note that none of the acicular, micrometer-scale Al_3Ti intermetallics, as observed in previous *post mortem* studies [12–16,16], are observed near the flux. This may suggest that the Al_3Ti phases precipitate during solidification [63,64], rather than as an intermediate state during the reaction as previously hypothesized [12,14,16,65]. However, given the relatively low solubility of Ti in Al [66], the unknown size of the Al_3Ti upon nucleation, and the additional complications due to Si, it is difficult to describe the role of the intermetallic conclusively. Nevertheless, the association between particle nucleation locations and Ti-rich regions may suggest that the flux plays a more direct role as the Ti source, although further confirmation of the relationship between the flux and Al_3Ti nucleation-dissolution is underway.

In summary, we have conducted a multi-modal, multi-scale correlative tomography investigation, combining real-time XRR and 2D (SEM) and 3D (TXM) observations, to identify the kinetics and formation mechanisms of flux-assisted reaction synthesis of Al-TiC MMCs. From XRR, we find that the carbide particle formation takes place in <600 s at 950 °C and appears to be nucleation- rather than growth dominated. We note also the absence of possible intermediary phases, *e.g.*, Al_3Ti, and also the proximity of the particles to the Ti-rich regions following flux reaction. From SEM and TXM, we discover that the particles form in a hexagonal platelet morphology with stepped interfaces. The presence of Si impurities may be responsible for this unexpected growth form. Despite the Si contamination, our work illustrates a promising first step towards real-time diagnostics and control of *in situ* MMC production. It is expected that our observations will inform the refinement of future correlative tomography campaigns and serve as a benchmark for future bulk processing experiments.

Declaration of Competing Interest

The authors declare that they have no known competing financial interests or personal relationships that could have appeared to influence the work reported in this paper.

Acknowledgments

The authors gratefully acknowledge financial support from the National Science Foundation (Award # 1762657) and from the University of Michigan College of Engineering. The authors also acknowledge technical support provided by the Michigan Center for Materials Characterization. We also thank David Weiss at Eck Industries and Steven Udvardy at the North American Die Casting Association for helpful discussions, as well as Jonathan Goettsch for experimental sample fabrication assistance. This research used resources of the Advanced Photon Source (APS), a U.S. Department of Energy (DOE) Office of Science User Facility operated for the DOE Office of Science by Argonne National Laboratory (ANL) under contract no. DE-AC02-06CH11357. This research also used resources of 18-ID of the National Synchrotron Light Source II (NSLS-II), a U.S. DOE Office of Science User Facility operated for the DOE Office of Science by Brookhaven National Laboratory (BNL) under contract no. DE-SC0012704.

Supplementary materials

Supplementary material associated with this article can be found, in the online version, at doi:10.1016/j.scriptamat.2021.113978.

References

[1] S.C. Tjong, Z.Y. Ma, Mater. Sci. Eng. 29 (2000) 49–113.
[2] N. Chawla, Y.L. Shen, Adv. Eng. Mater. 3 (6) (2001) 357–370.
[3] P. Krizkik, M. Balog, I. Matko, P.Svec Sr, M. Cavojsky, F. Simancik, J. Compos. Mater. 50 (1) (2016) 99–108.
[4] R.F. Guo, Y. Wang, P. Shen, A. Shaga, Y.H. Ma, Q.C. Jiang, Mater. Sci. Eng. A 775 (2020) 138956.
[5] K.B. Lee, H.S. Sim, H. Kwon, Metall. Mater. Trans. A 36 (2005) 2517–2527.
[6] J. Hashim, L. Looney, M.S.J. Hashmi, J. Mater. Process. Technol. 119 (2001) 324–328.
[7] I.A. Ibrahim, F.A. Mohamed, E.J. Lavernia, J. Mater. Sci. 26 (1991) 1137–1156.
[8] B.S.S. Daniel, V.S.R. Murthy, G.S. Murty, J. Mater. Process. Technol. 68 (1997) 132–155.
[9] I. Anza, M.M. Makhlouf, Metall. Mater. Trans. B 49 (2018) 466–480.
[10] H. Ding, H. Jia, W. Chu, Q. Liu, K. Chu, J. Wang, J. Mater. Res. Technol. 9 (3) (2020) 3865–3874.
[11] C.W. Reese, A. Gladstein, J.M. Fedors, V. De Andrade, B. Mishra, A.J. Shahani, A.I. Taub, Metall. Mater. Trans. A 51 (2020) 3587–3600.
[12] Y. Birol, J. Alloy. Compd. 454 (2008) 110–117.
[13] C. Cao, H. Ling, N. Murali, X. Li, Materialia 7 (2019) 100425.
[14] Y. Birol, J. Alloy. Compd. 455 (2008) 164–167.
[15] P. Baumli, J. Sytchev, G. Kaptay, J. Mater. Sci. 45 (2010) 5177–5190.
[16] Z. Liu, P. Xie, M. Chen, Q. Zheng, Y. Liu, X. Kai, Mater. Lett. 285 (2012) 129192.
[17] N. Samer, J. Andrieux, B. Gardiola, N. Karnatak, O. Martin, H. Kurita, L. Chaffron, S. Gourdet, S. Lay, O. Dezellus, Compos. Part A Appl. Sci. Manuf. 72 (2015) 50–57.
[18] L. Conteras, X. Turrillas, G.B.M. Vaughan, Å. Kvick, M.A. Rodríguez, Acta Mater. 52 (2004) 4783–4790.
[19] H. Boutefnouchet, C. Curfs, A. Triki, A. Boutefnouchet, D. Vrel, Powder Technol. 217 (2012) 443–450.
[20] J. Andrieux, B. Gardiola, O. Dezellus, J. Mater. Sci. 53 (2018) 9533–9544.
[21] F. Charlot, F. Bernard, E. Gaffet, D. Klein, J.C. Niepce, Acta Mater. 47 (2) (1999) 619–629.
[22] B. Winkler, D.J. Wilson, S.C. Vogel, D.W. Brown, T.A. Sisneros, V. Milman, J. Alloy. Compd. 441 (2007) 374–380.
[23] D.P. Riley, E.H. Kisi, T.C. Hansen, A.W. Hewat, J. Am. Ceram. Soc. 85 (10) (2002) 2417–2424.
[24] M.J. Mas-Guindal, X. Turrilas, T. Hansen, M.A. Rodríguez, J. Euro, Ceram. Soc. 28 (15) (2008) 2975–2982.
[25] A.J. Shahani, X. Xiao, E.M. Lauridsen, P.W. Voorhees, Mater. Res. Lett. 8 (12) (2020) 462–476.
[26] T.J.A. Slater, R.S. Bradley, G. Bertali, R. Geurtz, S.M. Northover, M.G. Burke, S.J. Haigh, T.L. Burnett, P.J. Withers, Sci. Rep. 7 (2017) 7332.
[27] M. Daly, T.L. Burnett, E.J. Pickering, O.C.G. Tuck, F. Léonard, R. Kelley, P.J. Withers, A.H. Sherry, Acta Mater. 130 (2017) 56–68.
[28] D. Tourret, J.C.E. Mertens, E. Lieberman, S.D. Imhoff, J.W. Gibbs, K. Henderson, K. Fezzaa, A.L. Deriy, T. Sun, R.A. Lebensohn, B.M. Batterson, A.J. Clarke, Metall. Mater. Trans. A 48 (2017) 5529–5546.
[29] A.J. Clarke, D. Tourret, Y. Song, S.D. Imhoff, P.J. Gibbs, J.W. Gibbs, K. Fezzaa, A. Karma, Acta Mater. 129 (2017) 203–216.
[30] J. Wang, P.D. Lee, R.W. Hamilton, M. Li, J. Allison, Scr. Mater. 60 (7) (2009) 516–519.

[31] A. Bjurenstedt, D. Casari, S. Seifeddine, R.H. Mathiesen, A.K. Dahle, Acta Mater. 130 (2017) 1–9.
[32] M. Ghahari, D. Krouse, N. Laycock, T. Rayment, C. Padovani, M. Stampanoni, F. Marone, R. Mokso, A.J. Davenport, Corros. Sci. 100 (2015) 23–35.
[33] C.S. Kaira, C. Kantzos, J.J. Williams, V. De Andrade, F. De Carlo, N. Chawla, Acta Mater. 144 (2018) 419–431.
[34] Y.K. Chen-Wiegart, S. Wang, Y.S. Chu, W. Liu, I. McNulty, P.W. Voorhees, D.C. Dunand, Acta Mater. 60 (2012) 4972–4981.
[35] X. Milhet, A. Nait-Ali, D. Tandiang, Y.J. Liu, D. Van Campen, V. Caccuri, M. Legros, Acta Mater. 156 (2018) 310–317.
[36] D. Roussel, A. Lichtner, D. Jauffrès, J. Villanova, R.K. Bordia, C.L. Martin, Scr. Mater. 113 (2016) 250–253.
[37] J. Schwartz, Y. Jiang, Y. Wang, A. Aiello, P. Bhattacharya, H. Yuan, Z. Mi, N. Bassim, R. Hovden, Microsc. Microanal. 25 (2019) 705–710.
[38] P. Thévenaz, U.E. Ruttimann, M. Unser, IEEE Trans. Image Process. 7 (1) (1998) 27–41.
[39] W.K. Lee, R. Reininger, W. Loo, R. Gambella, S. O'Hara, Y.S. Chu, Z. Zhong, J. Wang, Proc. SPIE 9592 (2015) 959209.
[40] B.A. Dowd, G.H. Campbell, R.B. Marr, V.V. Nagarkar, S.V. Tipnis, L. Axe, D.P. Siddons, Proc. SPIE 3772 (1999) 224–236.
[41] D.M. Pelt, V. De Andrade, Adv. Struct. Chem. Imaging 2 (2017) 1–14.
[42] D. Gürsoy, F. De Carlo, X. Xiao, C. Jacobsen, J. Synchrotron Radiat. 21 (2014) 118–1193.
[43] B.X. Dong, H.Y. Yang, F. Qiu, Q. Li, S.L. Shu, B.Q. Zhang, Q.C. Jiang, Mater. Des. 181 (2019) 107951.
[44] D. Zhou, S. Jin, Y. Li, F. Qiu, F. Deng, J. Wang, Q.C. Jiang, CrystEngComm 15 (2013) 643–649.
[45] S.B. Li, W.H. Xiang, H.X. Zhai, Y. Zhou, Powder Technol. 185 (2008) 49–53.
[46] R. Yu, Q. Zhan, L.L. He, Y.C. Zhou, H.Q. Ye, Acta Mater. 50 (2002) 4127–4135.
[47] K.J. Lijay, J.D.R. Selvam, I. Dinaharan, S.J. Vijay, Trans. Nonferrous Met. Soc. 26 (7) (2016) 1791–1800.
[48] J. Nie, X. Liu, X. Ma, J. Alloy. Compd. 491 (2010) 113–117.
[49] Q. Liu, F.G. Qi, X.L. Wang, H.M. Ding, Y. Shi, J. Ceram. Sci. Technol. 08 (4) (2017) 493–498.
[50] R. Yu, L.L. He, H.Q. Ye, Acta Mater. 51 (2003) 2477–2484.
[51] Z.M. Sun, Int. Mater. Rev. 56 (3) (2011) 143–166.
[52] C.C. Chen, T.Y. Huang, H.Z. Wu, Mater. Chem. Phys. 113 (2012) 1137–1143.
[53] Z.J. Lin, M.J. Zhuo, Y.C. Zhou, M.S. Li, J.Y. Wang, Acta Mater. 54 (2006) 1009–1015.
[54] Y.C. Zhou, J.X. Chen, J.Y. Wang, Acta Mater. 54 (2006) 1317–1322.
[55] Z.J. Lin, M.J. Zhuo, Y.C. Zhou, M.S. Li, J.Y. Wang, Scr. Mater. 55 (2006) 445–448.
[56] Y. Chu, S. Jing, D. Liu, J. Liu, Y. Zhao, Acta Mater. 162 (2019) 284–291.
[57] A.E. Standage, M.S. Gani, J. Am. Ceram. Soc. 50 (2) (1967) 101–105.
[58] Y.P. Zaykov, A.V. Isakov, I.D. Zakiryanova, O.G. Reznitskikh, O.V. Chemezov, A.A. Redkin, J. Phys. Chem. B 118 (2014) 1584–1588.
[59] Y. Du, Y.A. Chang, B. Huang, W. Gong, Z. Jin, H. Xu, Z. Yuan, Y. Liu, Y. He, F.Y. Xie, Mater. Sci. Eng. A 363 (2003) 140–151.
[60] B.L. Henke, E.M. Gullikson, J.C. Davis, At. Data Nucl. Data Tables 54 (2) (1993) 181–342.
[61] L. Svendsen, A. Jarfors, Mater. Sci. Technol. 9 (11) (1993) 948–957.
[62] K. Landry, S. Kalogeropoulou, N. Eustathopoulos, Mater. Sci. Eng. A 254 (1998) 99–111.
[63] L. Arnberg, L. Bäckerud, H. Klang, Met. Technol. 9 (1982) 7–13.
[64] M.S. Lee, B.S. Terry, Mater. Sci. Tech. 7 (1991) 608–612.
[65] E. Zhang, S. Zeng, B. Yang, Q. Li, M. Ma, Metall. Mater. Trans. A 30 (1999) 1147–1151.
[66] J.C. Schuster, M. Palm, J. Phase Equilibria Diffus. 27 (3) (2006) 255–277.